

SN 2023fyq: direct detection of a Type Ibn supernova progenitor and its multi-wavelength environmental constraints

Xinyi Hong^{1,2}, Ning-Chen Sun^{1,2,3*}, Yali Shao⁴, Ke Wang^{5,6}, Junjie Wu^{2,1}, Qiang Xi^{1,2}, Yi-Han Zhao^{1,2}, Justyn Maund⁷, Xiaohan Chen^{2,8}, Anyu Wang^{1,2}, Linxi Zhang^{1,2}, and Jifeng Liu^{2,1,3,9}

¹ School of Astronomy and Space Science, University of Chinese Academy of Sciences, Beijing 100049, China

² National Astronomical Observatories, Chinese Academy of Sciences, Beijing 100101, China

³ Institute for Frontiers in Astronomy and Astrophysics, Beijing Normal University, Beijing 102206, China

⁴ School of Space and Earth Sciences, Beihang University, Beijing 100191, China

⁵ Kavli Institute for Astronomy and Astrophysics, Peking University, Beijing 100871, China

⁶ Department of Astronomy, School of Physics, Peking University, Beijing 100871, China

⁷ Department of Physics, Royal Holloway, University of London, Egham, TW20 0EX, United Kingdom

⁸ School of Physics and Astronomy, China West Normal University, Nanchong 637002, China

⁹ New Cornerstone Science Laboratory, National Astronomical Observatories, Chinese Academy of Sciences, Beijing 100012, People's Republic of China

May 25, 2026

ABSTRACT

Context. Type Ibn supernovae (SNe) are characterized by narrow helium emission lines arising from ejecta-circumstellar medium interaction, yet their progenitors remain debated, with both massive Wolf-Rayet stars and low-mass helium stars in binaries proposed. **Aims.** We aim to directly identify the progenitor of the Type Ibn SN 2023fyq and to characterize its environment in order to constrain the progenitor's nature and evolutionary channel.

Methods. We search for the SN progenitor based on pre-explosion and late-time HST and JWST images and derive its properties by fitting the spectral energy distribution. We investigate the SN environment by probing the stars, dust, ionized gas and molecular gas with a multi-wavelength dataset including HST and JWST imaging, VLT/MUSE integral-field-unit spectroscopy and ALMA CO (2–1) radio interferometry.

Results. We discover a pre-explosion source at the SN position, which is consistent with a hot ($T > 15000$ K) and luminous ($\log(L/L_{\odot}) \geq 5.5$) SN progenitor and a possible host star cluster. The progenitor is confirmed to have disappeared after explosion. Analysis of the SN environment implies that the progenitor likely has an age of $\log(t/\text{yr}) = 7.1\text{--}7.2$. These phenomena disfavor a very massive single-star progenitor and instead support a binary scenario involving a low-mass helium star and a compact object; the observed progenitor emission likely arises from binary interaction that began at least ~ 12 yr before the explosion.

Conclusions. SN 2023fyq is the first Type Ibn SN with a directly detected progenitor and a possible host star cluster. It adds to the diversity of Type Ibn SNe in terms of their progenitor channels and mass-loss mechanisms.

Key words. supernova – supernova progenitor – environmental analysis

1. Introduction

Supernovae (SNe) are violent explosive events that denote the terminal phase of stars' life. They serve as a crucial driving force for cosmic nucleosynthesis, galactic chemical evolution, and energy feedback to the interstellar medium. SNe can be classified into several distinct types according to their spectral characteristics. The Type Ibn classification was first proposed by Pastorello et al. (2007), with SN 1999cp recognized as the first confirmed Type Ibn SN (Matheson et al. 2000). The defining feature of this type is the presence of narrow helium emission lines in their spectra with no-to-weak hydrogen lines. These narrow emission features are considered to arise from the interaction between SN ejecta and circumstellar material (CSM) expelled by the progenitor star shortly before the explosion (Hosseinzadeh et al. 2017; Pastorello et al. 2008). Therefore, the study of Type Ibn SNe is of vital importance to reveal the late mass-loss processes of the hydrogen-poor stripped stars.

Owing to the efficient conversion of extensive kinetic energy into radiative energy through CSM-interaction, Type Ibn SNe are typically more luminous than normal stripped-envelope SNe (Types IIb/Ib/Ic). Their peak absolute magnitudes generally span from -17 to -20 mag (Karamehmetoglu et al. 2017; Wang et al. 2024, 2025). Meanwhile, the light curves of SNe Ibn are relatively fast-evolving, with rise times of ~ 10 days and decline rates of ~ 0.1 mag/day (Farias et al. 2025; Cai et al. 2026). The light curves of Type Ibn SNe show a surprisingly high degree of homogeneity in contrast to the hydrogen-rich CSM-interacting Type IIn SNe, whose light curves are much more heterogeneous (Hosseinzadeh et al. 2017; Smith 2017).

The traditional view holds that Type Ibn SNe originate from massive ($>25 M_{\odot}$) Wolf-Rayet (WR) stars or stars transitioning from the luminous blue variable (LBV) phase to the WR phase (Foley et al. 2007). However, recent studies have shown that Type Ibn SNe are not always found in star-forming regions (Hosseinzadeh et al. 2019) or have a relatively low ejecta mass (Farias et al. 2025), implying the existence of an alternative

* Corresponding author: sunnc@ucas.ac.cn

evolutionary channel involving low-mass binary systems. For SN2015G, the progenitor were not detected on pre-explosion images, and the derived upper limit ruled out a single massive WR star (Shivvers et al. 2017). For SN2006jc, Maund et al. (2016) and Sun et al. (2020) reported a binary companion detection of its progenitor, strongly suggesting a not-so-massive progenitor in a binary system. Also, Dessart et al. (2022) conducted detailed spectral synthesis of several Type Ibn SNe and proposed that the progenitor could be a low-mass helium star in a binary system. Collectively, this growing body of observational and theoretical evidence indicates that the progenitors of Type Ibn SNe may be indeed low-mass binaries instead of single massive WR stars. However, it still remains an unresolved question whether there is any diversity in the progenitor channels of Type Ibn SNe and what mechanisms drive their violent pre-explosion mass loss. Till now, no progenitors have ever been directly detected on pre-explosion images for any Type Ibn SNe.

Discovered on April 17, 2023 (JD = 2460051.81897), SN2023fyq is a Type Ibn SN in the galaxy NGC4388 (De 2023) with a distance of 18 ± 3.7 Mpc (distance module $\mu = 31.28 \pm 0.45$ mag, Tully et al. 2016). SN2023fyq was initially classified as an Type Ib-pec (peculiar Type Ib) SN (Valerin et al. 2023), but later was identified as an Type Ibn SN based on its luminosity and spectral evolution (Brennan et al. 2024). Several works have conducted extensive multi-band photometric and spectroscopic follow-up observations. As noted by Dong et al. (2024), the evolution of SN2023fyq can be divided into four critical phases. From around $t = -1300$ to -100 d relative to the r -band maximum, SN2023fyq exhibits relatively steady precursors of ~ 20 mag. From $t = -100$ d, the precursor emission gradually brightens to ~ 16 mag until SN2023fyq exploded at $t = -11$ d. The "main" SN light curve shows a double-peaked profile, with the first peak powered by shock breakout (SBO) and the second by ejecta-CSM interaction. At the second peak, SN2023fyq reached its r band maximum of ~ 13 mag. From $t = 20$ days after maximum, the SN light curve shows a linear tail powered mainly by radioactive decay.

In addition, Dong et al. (2024) found that there were still strong medium-width helium lines in the nebular spectrum of SN2023fyq at ~ 136.8 ds, indicating that the ejecta-CSM interaction remained active in the late phase after the explosion. Baer-Way et al. (2025) reported the first radio view of a Type Ibn SN in SN2023fyq. They fit the radio emission from 58-185 days with a CSM of density $\sim 10^{-18}$ g/cm³ at a radius of 10^{16} cm, corresponding to a mass-loss rate of $\sim 4 \times 10^{-3} M_{\odot}/\text{yr}$ at 0.7-3 years before the explosion. Meanwhile, their late-time (at 525 days) non-detections in both radio and X-ray bands suggested a dense shell-like CSM with a width of at most 4×10^{15} to 2×10^{16} cm.

These observations suggest that the progenitor of SN2023fyq is extremely unstable before the explosion with a violent mass-loss process. Dong et al. (2024) proposed that the progenitor is likely a binary system comprising a low-mass helium star and a compact object. Precursor emission was attributed to mass transfer driven by the expansion of the helium star; during this phase, an equatorial accretion disk may have formed with a mass of approximately $0.6 M_{\odot}$. The ultimate explosion was possibly triggered either by core collapse of the helium star or by merger-induced instability of the binary system. Tsuna et al. (2024) also established a binary merger model of a low-mass helium star and a neutron star companion with an initial orbital period of 100 days, which successfully matched the observations of SN2023fyq. The radio data from Baer-Way et al. (2025) are also consistent with predictions from this merger model.

In this work, we report the direct detection of the progenitor of SN2023fyq, as well as a possible host star cluster, based on images taken by the Hubble Space Telescope (HST) and the James Webb Space Telescope (JWST). We note that K. Taggart et al. have independently discovered a progenitor candidate for SN2023fyq and reported it at the *Transients From Space* workshop¹; at that moment, however, it was not clear whether the candidate has disappeared after explosion; furthermore, no published study has systematically analyzed its progenitor and environment. As will be shown in this paper, we find that at late times SN2023fyq has become much fainter than the progenitor candidate; this confirms that the candidate is the genuine progenitor and has disappeared after explosion. Study of the SN environment can also provide key insights into their progenitors (e.g. Sun et al. 2023b; Xi et al. 2025, 2026; Niu et al. 2026). Therefore, we perform a detailed analysis of the host galaxy and local environment of SN2023fyq based on HST and JWST imaging, integral-field-unit (IFU) spectroscopy by the Multi Unit Spectroscopic Explorer (MUSE) on the Very Large Telescope (VLT), and CO (2–1) radio interferometry by the Atacama Large Millimeter/sub-millimeter Array (ALMA). Our aim is to reveal and understand what progenitor gives rise to this SN and derive its key parameters.

As mentioned, all epochs in this paper are relative to the r -band maximum of SN2023fyq at JD = 2,460,154.3 \pm 0.5 (Dong et al. 2024) unless otherwise specified. We shall use a Galactic reddening of $E(B - V)_{\text{MW}} = 0.029$ mag and a host-galaxy distance of 18 ± 3.7 Mpc, both consistent with Dong et al. (2024). This paper is organized as follows. Observations we used are described in Section 2. We search for and analyze the progenitor in Section 3, and investigate the SN environment in Section 4. We finally summarize and discuss the main results in Section 5.

2. Data

2.1. HST and JWST imaging

In this work, we used images from HST and JWST, the complete information for which is presented in Table 1. The HST observations were conducted by the Wide Field Camera 3 (WFC3) in both the Ultraviolet-Visible (UVIS) channel and the Infrared (IR) channel, spanning a wide wavelength from the F336W band to the F160W band. Most of the observations were conducted in 2011, i.e. ~ 12 years before the explosion of SN2023fyq, except one F336W observation that was performed at late times in 2025, i.e. ~ 2 years post explosion.

The SN site was also observed by JWST with the Near-Infrared Camera (NIRCam) and the Mid-Infrared Instrument (MIRI). The MIRI observations were conducted in the F560W, F1000W, F1500W, F1800W, F2100W and F2550W filters at two epochs in June 2023 and June 2024, corresponding to $t = -31$ days (during the outburst phase before core collapse) and $t = 321$ days relative to the r -band maximum of SN2023fyq; we shall use the F1800W images to locate the SN position (see Section 3.1) while those in the other filters are not used in this work. The NIRCam observations were taken in the F182M and F335M filters in January 2025, or $t = 531$ ds after the r -band maximum. We shall use the NIRCam images to study the SN environment.

¹ <https://www.stsci.edu/contents/events/stsci/2025/march/transients-from-space>; <https://www.youtube.com/watch?v=NpIV632xgR8>.

All the above data were obtained from Mikulski Archive for Space Telescopes (MAST)². Photometry was performed with DOLPHOT (Dolphin 2000, 2016). We used `FitSky` = 2 and `RAper` = 3, which are recommended by the user manual for crowded regions. We set `Force1` = 1 (force all objects to be fitted as stars) and `ApCor` = 1 (turn on aperture correction) for better point-source photometry. For HST/WFC3 we used `UseWCS` = 1 to perform image alignment based on the header information of the world coordinate system (WCS) while for JWST/NIRCam we used `UseWCS` = 2 since the DOLPHOT/NIRCAM module does not include the default distortion parameters. In addition, we used `WFC3useCTE` = 0 for HST/WFC3/UVIS and `WFC3useCTE` = 1 for HST/WFC3/IR because images of the former have already been corrected for charge transfer inefficiency on the pixel level while those of the latter have not. All other parameters are the same as recommended by the DOLPHOT user manual.

2.2. VLT/MUSE IFU spectroscopy

The host galaxy of SN 2023fyq was observed with VLT/MUSE in March 2022 (Program ID: 108.229J.001; PI: Venturi, Giacomo). The observations were carried out in the wide-field mode (WFM) with extended wavelength setting, covering a field of view of $1' \times 1'$ at a spatial sampling of $0.2''$ and a wavelength range 4700 \AA to 9350 \AA at a spectral sampling of 1.25 \AA . The total exposure time was 4440 s with two equal-duration exposures. The raw data have been well reduced by the standard pipeline, and we retrieved the calibrated datacube from the European Southern Observatory (ESO) data archive³.

We used the IFUANAL package⁴ to further process the datacube. The datacube was first corrected for Galactic extinction and deredshifted. Then, to mask and remove the stellar continuum in the galaxy, the spaxels were binned using Voronoi tessellation to achieve signal-to-noise ratios of at least 120 over the wavelength range 5590 \AA to 5680 \AA . In each bin, we fitted the spectrum with the STARLIGHT package (Cid Fernandes et al. 2005) based on the Bruzual & Charlot (2003) stellar population models. Therefore, the stellar continuum was able to be masked and subtracted from the spectrum, leaving only the gaseous component in the datacube.

2.3. ALMA CO (2–1) radio interferometry

We adopted the ALMA CO (2–1) observations using the 7-m array toward NGC 4388. These observations were conducted on December 22, 2019 with 10 antennas (ID: 2019.1.00763.L) and April 27 and 28, 2024 with 11 antennas (ID: 2023.1.00026.S), respectively. The on-source integration time was 15 and 21 min, respectively. The flux density scale was established using scans of the standard calibrators J1058+0133 and J1256-0547 (ID: 2019.1.00763.L), and 1229+0203 (ID: 2023.1.00026.S). The phase and water vapour were further checked by observing the nearby calibrators of J1215+1654 (ID: 2019.1.00763.L), and J1222+0413 and J1254+1141 (ID: 2023.1.00026.S).

We retrieved data from the ALMA science archive⁵ and performed calibration with the standard pipeline and the CASA pack-

age⁶. We only considered the frequency range overlapping with our science goals for the final combination of multi-execution data. We made the line datacube from the combined calibrated data using the TCLEAN task with Briggs weighting and `robust` = 0.5 (in order to optimize the sensitivity per frequency bin and the resolution of the final map), and with `auto-multithresh` mask and `side-lobethreshold` = 2.0, `noisethreshold` = 4.25, `minbeam-frac` = 0.3, `lownoisethreshold` = 1.5, `negativethreshold` = 15.0, and `threshold` = 3σ in a gridder mode of mosaic. The synthesized beam size is $7.4'' \times 4.4''$, corresponding to $646 \text{ pc} \times 384 \text{ pc}$ at the host galaxy's distance. The noise level in a 15.625 MHz channel is $\sim 5.5 \text{ mJy beam}^{-1}$, and the moment-0 map (i.e. the velocity-integrated intensity) has a sensitivity of $\sim 1 \text{ Jy beam}^{-1} \text{ kms}^{-1}$.

3. Progenitor Detection

3.1. Identification and photometry

Fig. 1(a) shows the HST F336W/F438W/F814W three-color composite image of the host galaxy NGC 4388. SN 2023fyq is located on one of the spiral arms at ~ 10 arcsec away from the galaxy center. The local SN environment is a very dense field with a large number of bright blue stars/clusters.

Fig. 1(b,c) compare the JWST/MIRI/F1800W images taken during the outburst phase shortly before core collapse ($t = -31$ d) and after the explosion of SN 2023fyq ($t = 321$ d). Near the reported SN coordinates, we find a point source with variable brightness, being significantly brighter after the SN explosion. We identify this source as SN 2023fyq. We then used the PHOTUTILS package⁷ to pinpoint the source positions and computed the coordinate transformation matrices across different images based on common stars; in this way, we determined the precise SN positions on all HST and JWST images.

On the pre-explosion HST images, a point source (labelled as *Source A*) is significantly detected at the SN position in all filters. As an example, Fig. 1(d) shows the pre-explosion image in the F336W band. At late times, *Source A* is still visible on the F336W image (Fig. 1e), but appears much fainter than the pre-explosion level, confirming that *Source A* is physically associated with SN 2023fyq.

Based on photometry with the DOLPHOT package, we obtained the magnitudes of *Source A* across multiple wavelength bands (Table 2). We can see clearly that the the brightness of *Source A* in the F336W band has faded from pre-explosion to late time, with a magnitude difference of $\Delta m = 0.925$ mag. Note that the two HST/WFC3/IR images in the F110W and F160W bands have relatively lower spatial resolutions and the detected source is likely contaminated by the close neighbours of *Source A*. We use the HST/WFC3/UVIS/F814W and JWST/NIRCAM/F182M images to resolve the stellar environment and estimate the contamination in the F110W and F160W bands with interpolation. The details can be found in Appendix A. The final spectral energy distribution (SED) of *Source A* is presented in Fig. 2.

3.2. Modeling the SED

Fig. 3(a) compares the pre-explosion and late-time brightness of *Source A* with the light curve of SN 2023fyq as reported by Dong et al. (2024). Our pre-explosion detection of *Source A* corresponds to $t = -4461 \sim -4433$ d, long before the first precursor

² <https://mast.stsci.edu/portal/Mashup/Clients/Mast/Portal.html>

³ <https://archive.eso.org/scienceportal/home>

⁴ <https://ifuanal.readthedocs.io/en/latest/index.html>

⁵ <https://almascience.nrao.edu/>

⁶ <https://casa.nrao.edu/>

⁷ <https://github.com/astropy/photutils>

Table 1: HST and JWST observations of SN 2023fyq used in this work.

Telescope	Proposal ID	Date	Epoch ^a (day)	Instrument	Filter	Exposure Time (s)
HST	12365	2011-05-11	-4461	WFC3/UVIS	FQ508N	574
		2011-05-11	-4461	WFC3/UVIS	F665N	474
		2011-05-11	-4461	WFC3/UVIS	F547M	194
		2011-05-11	-4461	WFC3/UVIS	F621M	194
		2011-05-11	-4461	WFC3/UVIS	F673N	306
	12185	2011-06-08	-4433	WFC3/IR	F110W	147
		2011-06-08	-4433	WFC3/IR	F160W	422
		2011-06-08	-4433	WFC3/UVIS	F336W	1230
		2011-06-08	-4433	WFC3/UVIS	F438W	410
		2011-06-08	-4433	WFC3/UVIS	F814W	1952
17535	2025-03-07	588	WFC3/UVIS	F336W	2328	
JWST	2064	2023-06-27	-31	MIRI	F1800W	358
	6659	2024-06-13	321	MIRI	F1800W	358
	5627	2025-01-10	532	NIRCAM	F182M	1632
		2025-01-10	532	NIRCAM	F335M	1632

Notes. PIs: 12365: Wang; 12185: Greene; 17535: Veilleux; 2064: Rosario; 6659: Taggart; 5627: Veilleux.

^(a) The epochs are with respect to the maximum light in the r band at $\text{JD} = 2,460,154.3 \pm 0.5$, as reported by Dong et al. (2024).

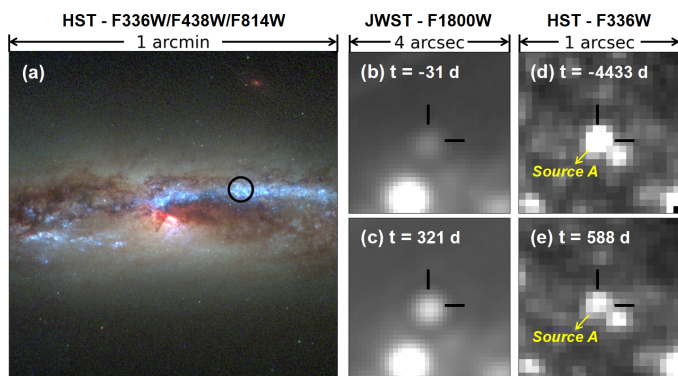


Fig. 1: (a) F336W/F438W/F814W three-colour composite image of the host galaxy by HST observations. The black circle shows the SN site. (b, c) JWST/MIRI/F1800W images of the SN site during the outburst phase and after the SN explosion. (d, e) Pre-explosion and late-time images taken by HST/WFC3/UVIS in the F336W band. The crosshairs mark the SN position. All images are aligned with North up and East to the left.

detections at $t = -2337$ d by Dong et al. (2024) using ground-based telescopes. The late-time HST/WFC3/UVIS/F336W detection of *Source A* corresponds to $t = 588$ d; at this epoch, SN emission should have already faded based on the decline rate of the SN light curve tail. While late-time emission powered by circumstellar medium (CSM) interactions cannot be entirely excluded (Fremling et al. 2026), Baer-Way et al. (2025) reported no radio detection at a similar phase, implying that any CSM present would be too diffuse to sustain detectable luminosity. We therefore assume that the SN flux had completely vanished at this time.

We model the pre-explosion SED of *Source A* as composed of a SN progenitor and a star cluster and the late-time SED as the cluster alone, assuming no more late-time radiation from the SN itself and that the progenitor has disappeared after the SN explosion. We suggest the presence of a star cluster due to the following reasons. (1) The F665N flux of *Source A* is much higher

Table 2: HST photometry of *Source A*.

Filter	Pre-explosion ($t = -4461 \sim -4433$ d)	Late-time ($t = 588$ d)
F336W	21.126 (0.020)	22.051 (0.036)
F438W	22.479 (0.037)	-
F547M	22.456 (0.042)	-
F621M	22.320 (0.045)	-
F665N	21.189 (0.043)	-
F673N	22.074 (0.099)	-
F814W	21.862 (0.023)	-
F110W	20.995 (0.063)	-
F160W	20.372 (0.069)	-

Notes. The F110W and F160W photometry is likely contaminated by some close neighbours due to the relatively lower spatial resolution of HST/WFC3/IR. See Appendix B for details. All magnitudes in this paper are in the VEGA photometric system.

than the continuum (Fig. 2) and suggests significant $H\alpha$ emission; since the progenitor of SN 2023fyq is hydrogen-poor, this emission is most likely due to ionized gas associated with a star cluster. (2) The F110W and F160W bands show a clear IR excess compared with the Rayleigh-Jeans tail extrapolated from bluer bands; this is naturally explained by the integrated emission from red supergiants (RSGs) within a star cluster. (3) *Source A* is located in a very dense stellar field (Fig. 1), where physical association or chance alignment with a star cluster could be very common.

We use blackbody models to fit the progenitor and Binary Population and Spectral synthesis (BPASS) models (Byrne et al. 2022) to fit the cluster; we adopt a SN host-galaxy reddening of $E(B - V)_{\text{host}} = 0.037 \pm 0.09$ mag as derived by Dong et al. (2024) and an extinction law of $R_V = 3.1$ (Cardelli et al. 1989). The best-fitting model spectra are displayed in Fig. 2. The cluster is found to have an age of $\log(t/\text{yr}) = 7.1 \pm 0.1$ and an initial mass of $\log(M/M_\odot) = 3.8^{+0.1}_{-0.1}$; the SN progenitor has a temperature of >15000 K, a luminosity of $\log(L/L_\odot) \gtrsim 5.5$ and a radius of $\log(R/R_\odot) \lesssim 2$.

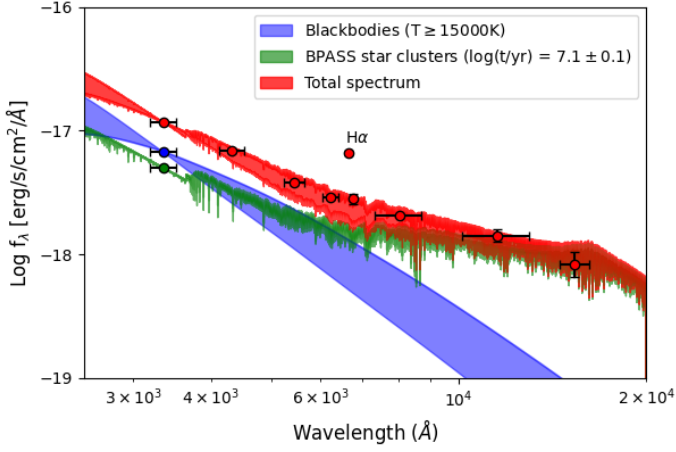


Fig. 2: Observed and model pre-explosion SEDs (red) of *Source A* and its two components, i.e. a SN progenitor modeled as a blackbody (blue) and a star cluster that persists after the SN explosion (green). The green data point corresponds to the late-time detection of *Source A* while the blue data point corresponds to the flux that has vanished from pre-explosion to late-time epochs. The horizontal error bars show the root-mean-square widths of the filters. For the F110W and F160W filters, the vertical error bars have accounted for the uncertainty due to contamination of neighbouring stars (see Appendix B for details) while for the other filters the vertical error bars reflect photometric uncertainties.

We also consider the possibility that the star cluster may be in chance alignment with the SN progenitor and has a different extinction from that derived by Dong et al. (2024) for the SN. As we shall show later in Section 4, there are two stellar populations in the SN environment. The extinction of the older stellar population is consistent with that of the SN, while the extinction of the younger stellar population is slightly higher. We performed another fitting using the extinction of the younger stellar population, and the derived cluster age does not change significantly. Furthermore, the cluster age is very consistent with that of the older stellar population; therefore, the star cluster is most likely to be part of the older stellar population with a lower extinction. As shall be discussed in Section 4.3, we suggest that this star cluster possibly hosts the progenitor of SN 2023fyq although chance alignment cannot be fully excluded.

Fig. 3(b–d) compares the blackbody parameters of the SN progenitor with those of SN 2023fyq from Dong et al. (2024). From the early pre-explosion phase to the precursor phase, the luminosity increased from $>10^{39}$ erg/s to $\sim 10^{40}$ erg/s, and the blackbody radius increased from $<100 R_{\odot}$ to $>400 R_{\odot}$, while its temperature decreased from $>15,000$ K to $<12,500$ K. Fig. 4 displays the possible position of the SN progenitor on the Hertzsprung–Russell (HR) diagram. The progenitor luminosity lies at the upper end of the possible luminosity range for single stars, close to some of the most luminous very massive stars of $>100 M_{\odot}$ in the Milky Way or in the Large Magellanic Cloud (Crowther et al. 2010). However, we deem it unlikely that the progenitor is a very massive star, which shall be discussed later.

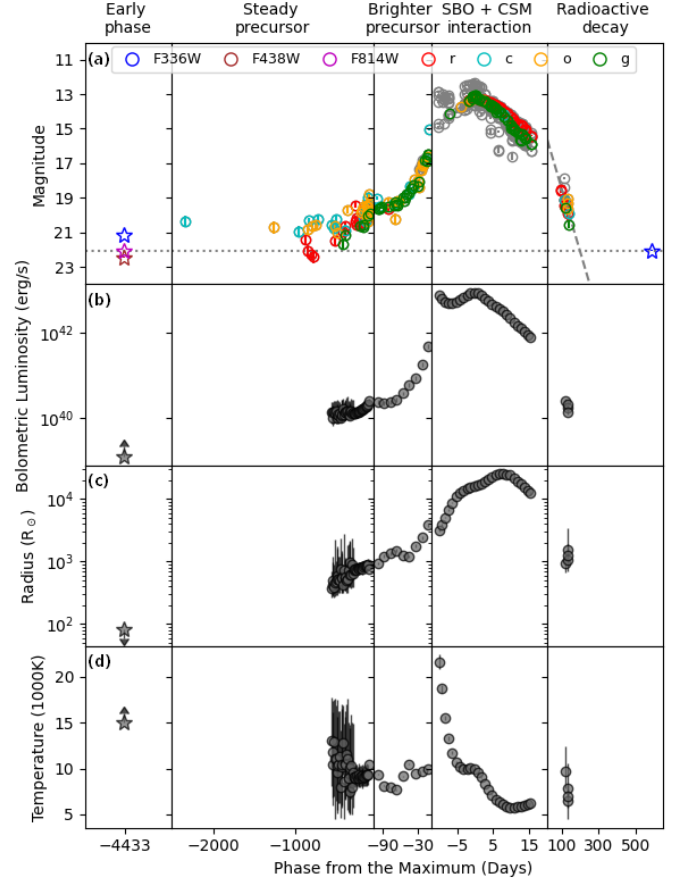


Fig. 3: The pre- and post-explosion evolution of the (a) magnitude, (b) bolometric luminosity, (c) blackbody radius and (d) temperature of SN 2023fyq. Stars correspond to detections in this work while circles are data from Dong et al. (2024). In the magnitude panels, colored circles correspond to different bands as shown in the legend above; gray circles represent magnitudes in other bands from Dong et al. (2024). The full evolution is divided into five critical phases according to Dong et al. (2024) and this work. Our detection is around 2100 d before the first precursor detections by Dong et al. (2024).

4. SN environment

4.1. Structure of the host galaxy

With the abundant data from HST, JWST, ALMA and VLT, we can analyze the structure of SN 2023fyq’s host galaxy in detail. It is worth noting that NGC 4388 has a nearly edge-on inclination of 79° (Damas-Segovia et al. 2016). Such a high inclination significantly increases line-of-sight dust extinction and further complicates optical-band analyses.

Fig. 5(a) shows the optical image of NGC 4388 by HST. We can see two spiral arms (labeled as the *Eastern Arm* and *Western Arm*), composed of blue and bright stars, as well as heavy dust obscuration on the disk. The spiral arms on both sides appear highly asymmetric: the *Western Arm* is more prominent and continuous, while the *Eastern Arm* is much fainter and patchy. This asymmetry is likely due to the different relative distributions of stars and dust along the line of sight; on the *Eastern Arm*, dust lies in the foreground relative to the stars, whereas the reverse is true for the *Western Arm*. Therefore, the *Eastern Arm* is heavily

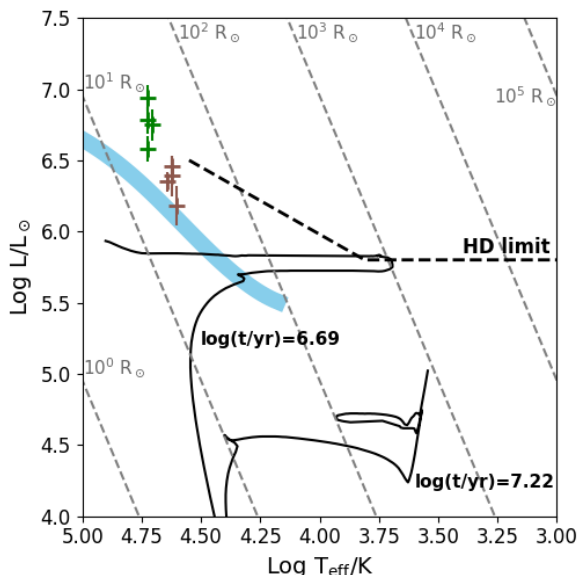


Fig. 4: Position of SN 2023fyq’s progenitor on the HR diagram (blue shaded region). The black solid lines are PARSEC v1.2S single stellar isochrones (Bressan et al. 2012), the reference ages of which are derived by environmental stellar populations fitting (see Section 4.2 for details). The black dashed line is the Humphreys & Davidson (1979) limit for stellar luminosity and the grey dashed lines correspond to constant blackbody radii. The “+” symbols show some of the most luminous stars in the Milky Way (NGC 3603-A1a, A1b, B and C; in brown) and the Large Magellanic Cloud (R136a1–3 and b; in green; Crowther et al. 2010).

obscured by the foreground dust while the *Western Arm* is much less affected.

Fig. 5(b) shows the near-IR F335M image by JWST. At this wavelength, dust extinction is much lower and stars behind dust can be more easily seen. Compared with the optical image, the *Eastern Arm* is much brighter and more continuous on the near-IR image and it is now more symmetric to the *Western Arm*. This confirms the speculation in the previous paragraph that foreground dust obscuration causes the faintness and patchiness of the *Eastern Arm* on the optical image.

ALMA has detected significant CO (2–1) molecular line emission across the host galaxy. As an example, the top panel of Fig. 6 shows the CO (2–1) line in the spectrum at the SN site. Fig. 5(c) presents the velocity-integrated intensity map of the CO (2–1) emission line by ALMA. There is a large amount of molecular gas at the galactic center and on the spiral arms. The spatial distribution is very symmetric on both spiral arms, which is similar to stellar distribution on the near-IR image (Fig. 5b) but very different from that on the optical image (Fig. 5a).

We further use the VLT/MUSE IFU datacube to analyze the ionized gas. As an example, the bottom panel of Fig. 6 shows the continuum-subtracted spectrum at the SN position. There are prominent emission lines H β , [O III], [N II] and H α in the spectrum. On the spiral arms, the line profiles can be well described by single-Gaussian profiles. In the nuclear region, however, the line profiles can be much more complicated with more than one, and sometimes even up to four, Gaussian components. This indicates that NGC 4388 has complex gas kinematics around the galaxy center, likely caused by active galactic nucleus (AGN) outflows and/or other nuclear activities (Fujiwara et al. 2026).

We fit the lines with single- or multi-Gaussian functions for all 2157 spaxel bins across the galaxy, examples of which can be found in Appendix B.

Fig. 5(d-f) shows maps of line integrated flux, central velocity and width for H α ; parameters of the narrowest component are adopted in case there are multiple components at a spaxel bin. Fig. 5(d) shows strong H α emission at the nuclear region and on both spiral arms. We adopt the Baldwin-Phillips-Terlevich (BPT) diagram to identify whether the emission lines originate from an AGN or star formation (see details in Appendix C). We find that the ionized gas on the spiral arms is excited by star formation while that in the nuclear region is by AGN.

The line central velocity map (Fig. 5e) shows a clear pattern of galactic disk rotation. The gas on the *Eastern Arm* is moving away from us along the line of sight (redshifted), while that on the *Western Arm* is moving towards us (blueshifted). Fig. 5(f) shows that most regions on the spiral arms have similar line widths of $\sim 1.2 \text{ \AA}$. This width is almost the same as the instrumental broadening (Guérou et al. 2017), indicating very low intrinsic velocity dispersion of the ionized gas.

We further used Balmer decrement to estimate the interstellar extinction (Fig. 5g), assuming an intrinsic flux ratio of H α /H β = 2.86 (Osterbrock & Ferland 2006) and a Fitzpatrick (2004) extinction law with $R_V = A_V/E(B - V) = 3.1$. Overall, we can observe that the extinction on the *Eastern Arm* is higher than that on the *Western Arm*, which is consistent with our earlier inference about the spatial distribution of objects within the galaxy. And the host extinction at the SN site is $A_V^{\text{host}} \sim 0.8 \text{ mag}$.

We estimate the gas-phase metallicity via the strong-line diagnostics, using the O3N2 calibration from Marino et al. (2013). Note that this calibration is based on HII regions instead of AGN-ionized gas. Therefore, we only derive the metallicity for the regions ionized by star formation (Fig. 5h). The spiral arms have a roughly uniform metallicity of $12 + \log(\text{O}/\text{H}) = 8.5 \pm 0.18 \text{ dex}$, which is slightly lower than the solar metallicity (8.69 dex, Asplund et al. 2009). This metallicity value has been utilized in the SED fitting of *Source A* (Section 3.2) and will be used the resolved stellar population fitting in the next section (Section 4.2).

4.2. Stellar populations in the local SN environment

With the high-resolution photometry data from HST, we can perform a quantitative analysis of the star-forming history in the local SN environment. Here we only use the wide filters of F336W, F438W and F814W. In a circular region with a radius of 100 pc around SN 2023fyq, we selected good stars based on the following criteria: (1) type of source, $\text{obj} = 1$; (2) signal-to-noise ratio, $\text{snr} > 5$; (3) source sharpness, $|\text{shp}| < 0.5$; (4) source crowding, $\text{crd} < 2$; (5) photometry quality flag, $\text{qfg} < 3$. We finally selected a catalog of 135 sources (excluding the progenitor candidate) for further analysis.

We performed artificial star tests to estimate the detection limits within the SN environment and calculate a scaling factor of the reported photometric uncertainty to account for the additional error introduced by source crowding (the method is the same as that in Hong et al. 2024). Fig. 7 shows the colour-magnitude diagrams (CMDs) drawn with the catalog. It can be seen that the photometric error caused by crowding is very large.

Based on this catalog, we use a hierarchical Bayesian approach (Maund & Ramirez-Ruiz 2016, Sun et al. 2021, 2022, 2023a,b, Niu et al. 2023) to fit the observed environmental stars with model stellar populations (based on PARSEC v1.2S stellar

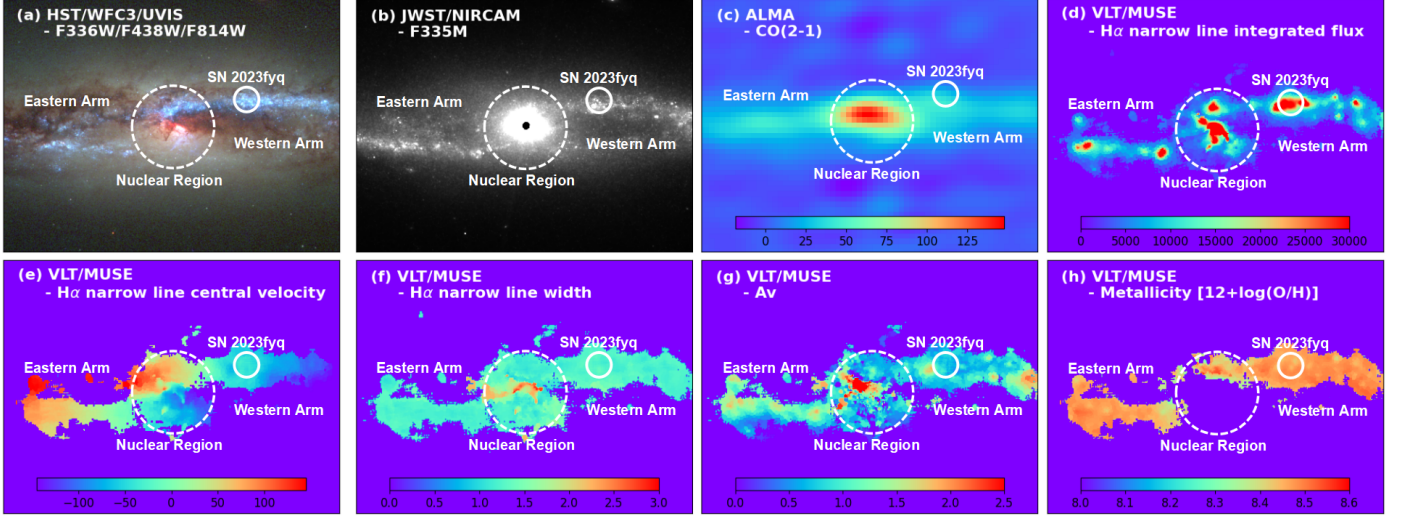


Fig. 5: Maps of SN 2023fyq’s host galaxy NGC 4388. (a) The F336W/F438W/F814W three-colour composite image observed by HST/WFC3/UVIS. (b) The F335M-band image observed by JWST/NIRCam. (c) The velocity-integrated intensity map of the CO (2–1) emission line observed by ALMA, in units of $\text{Jy beam}^{-1} \text{ km s}^{-1}$. (d) The wavelength-integrated flux map of the $\text{H}\alpha$ narrow emission line observed by VLT/MUSE, in units of $10^{-20} \text{ erg s}^{-1} \text{ cm}^{-2}$. (e) The $\text{H}\alpha$ line central velocity map in units of km s^{-1} . (f) The $\text{H}\alpha$ line width map in units of \AA . (g) The host extinction map in units of mag. (h) The $12 + \log(\text{O}/\text{H})$ metallicity map in units of dex. In (d–h), only parameters of the narrowest component are displayed when there are multiple Gaussian components in the line profile in a spaxel. The solid circles show the location of SN 2023fyq and the dashed circles mark the *Nuclear Region* with the *Eastern Arm* and *Western Arm* located on either side of it. All panels are aligned with North up and East to the left.

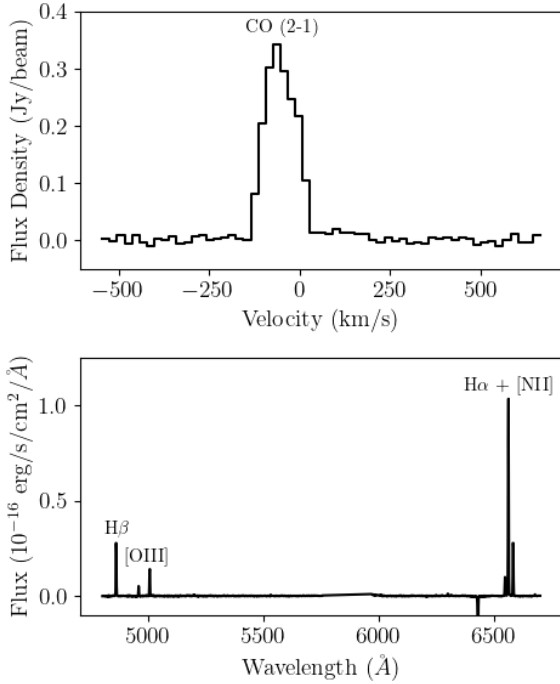


Fig. 6: *Top*: molecular line emission of CO (2–1) at the position of SN 2023fyq as observed by ALMA; the host galaxy’s redshift has been corrected and the blueshift of the line center reflects the galaxy’s disk motion toward the observer. *Bottom*: VLT/MUSE spectrum at the SN position with the stellar continuum subtracted; the host galaxy’s redshift and Galactic foreground reddening have been corrected.

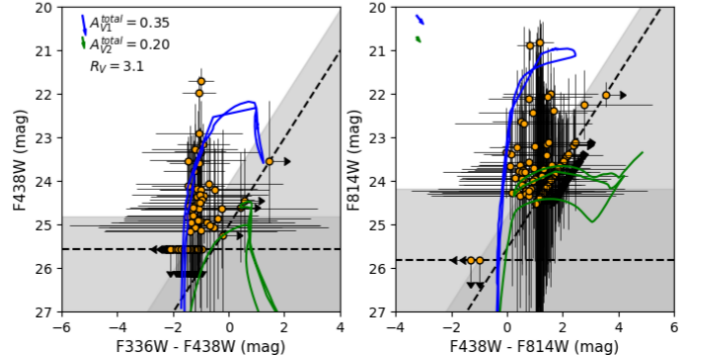


Fig. 7: CMDs of all stellar sources in the local environment of SN 2023fyq. In both panels, the blue and green isochrones correspond to stellar populations with $\log(t/\text{yr}) = 6.69$ and 7.22 , respectively. The arrows in the upper-left corner, color-matched to each isochrone, represent reddening vectors for $R_V = 3.1$ and total extinctions of $A_V^{\text{total}} = 0.35$ and 0.20 (which correspond to best-fitting host extinctions of $A_V^{\text{host}} = 0.26$ and 0.11 for the two populations, respectively, in addition to a Milky Way reddening of $E(B - V)_{\text{MW}} = 0.029$ mag).

isochrones⁸, Bressan et al. 2012). We find that the environmental stars can be well fitted with two model stellar populations, one with an age of $\log(t/\text{yr}) = 6.69^{+0.01}_{-0.01}$ and a host extinction of $A_V^{\text{host}} = 0.26^{+0.09}_{-0.07}$ and the other with $\log(t/\text{yr}) = 7.22^{+0.02}_{-0.02}$ and $A_V^{\text{host}} = 0.11^{+0.02}_{-0.02}$.

⁸ <http://stev.oapd.inaf.it/cgi-bin/cmd>

4.3. A simple picture of the SN environment

In Section 4.1 we have already shown the distribution of stars on the optical and near-IR images as well as the molecular gas and ionized gas in the host galaxy of SN 2023fyq. A key phenomenon is that the spiral arms traced by stars are highly asymmetric on the optical images, while on the near-IR images they are much more symmetric. As previously suggested, this is most likely due to different relative distributions of stars and dust along the line of sight: dust resides in front of stars on the *Eastern Arm* and causes much higher obscuration, while on the *Western Arm* most dust is in the background of stars and has a much smaller influence.

In the local SN environment, we find two stellar populations (Section 4.2). The older population has lower host extinction ($A_V^{\text{host}} = 0.11$ mag) compared to the younger population ($A_V^{\text{host}} = 0.26$ mag). In contrast, the ionized gas shows a noticeably higher extinction ($A_V^{\text{host}} = 0.8$ mag) than both stellar components (Section 4.1; Fig. 5g). This indicates that, along the line of sight at the SN site, the components ordered from near to far are the older stellar population, the younger stellar population, and ionized gas, so that they have increasingly higher interstellar extinctions. The molecular gas (Fig. 4.1c) is most likely to reside in the background of the ionized gas since otherwise the large amount of dust in the molecular clouds would obscure the light of the other components.

Based on the above discussion, we suggest a 3-dimension structure of the host galaxy as illustrated by Fig. 8. This 3-dimensional structure is consistent with a scenario in which spiral arms trigger sequential star formation as gas propagates through its potential well. Note that, on the *Western Arm*, gas is moving toward the observer along the line of sight (Fig. 5e) and that SN 2023fyq, at a distance of only ~ 0.9 kpc from the galaxy center, is most likely to reside within the spiral arm-disk corotation radius (which is typically $\gtrsim 4$ kpc for a NGC4388-like galaxy; Abdeen et al. 2020; Marchuk 2024; Kostjuk et al. 2024, 2025). Therefore, the molecular gas near the SN site moves faster than the spiral arm and it propagates through the spiral arm from behind; during this process, gas gets compressed, forming stars, and is then ionized by the ultraviolet radiation of the newly formed stars. This mechanism leads to a sequence of molecular gas, ionized gas, younger stars and older stars at different positions relative to the spiral arms, as shown in Fig. 8 for NGC 4388 and often seen in many other galaxies (Hou & Han 2015).

In Section 3 we have detected a pre-explosion source at the SN position and modeled its SED as a SN progenitor with a star cluster. The age of the star cluster derived from the SED fitting is $\log(t/\text{yr}) = 7.1 \pm 0.1$, which is very close to the age of the older stellar population ($\log(t/\text{yr}) = 7.22^{+0.02}_{-0.02}$) obtained by fitting the resolved stellar populations in the local SN environment (Section 4.2). As for the SN progenitor, Dong et al. (2024) have obtained a host-galaxy reddening of $E(B - V)_{\text{host}} = 0.037 \pm 0.09$ mag, or an extinction of $A_V^{\text{host}} = 0.11$ mag, using the Na I D absorption doublets. This is also very close to the extinction of the older stellar population in the local SN environment ($A_V^{\text{host}} = 0.11$ mag), but much lower than that of the younger stellar population ($A_V^{\text{host}} = 0.26$ mag). Therefore, it is very likely that both the SN progenitor and the star cluster are members of the older stellar population so that they share similar ages and interstellar extinctions; it is also possible that the star cluster hosts the SN progenitor, although chance alignment cannot be entirely excluded. Based on the above discussion, we conclude that the progenitor of SN 2023fyq has an age of $\log(t/\text{yr}) = 7.1-7.2$.

5. Summary and discussion

SN 2023fyq is a Type Ibn SN in the nearby galaxy NGC 4388. In this paper, we perform a detailed analysis of its progenitor and environment based on HST and JWST imaging, VLT/MUSE IFU spectroscopy, and ALMA CO(2-1) radio interferometry.

On the pre-explosion HST images, we detect a point source at the SN position in all the observed bands from F336W to F160W. Its brightness in F336W significantly faded from pre-explosion to late times, confirming that this source is physically associated with the SN. We attribute this dimming to a SN progenitor that has disappeared and the remaining late-time brightness to a star cluster. Under this assumption, the pre-explosion source can be modeled as the combination of a hot progenitor, with a temperature of >15000 K, a luminosity of $\log(L/L_{\odot}) \gtrsim 5.5$ and a radius of $\log(R/R_{\odot}) \lesssim 2$, and a star cluster with an age of $\log(t/\text{yr}) = 7.1 \pm 0.1$. This makes SN 2023fyq the first Type Ibn SN with a directly detected progenitor and a possible host star cluster.

Meanwhile, we carried out a detailed analysis of the SN host galaxy by probing the stars, ionized gas and molecular gas with the multi-wavelength dataset. In the local SN environment, we found two stellar populations with different ages and extinctions. Based on these observations, we suggest a 3-dimensional structure of the host galaxy, in which spiral arms trigger sequential star formation as gas propagates through its potential well. The SN progenitor that we have identified on the pre-explosion images is most likely to be associated with the older stellar population and have an age of $\log(t/\text{yr}) = 7.1-7.2$.

On the HR diagram, the position of SN 2023fyq's progenitor is consistent with a single very massive star of $>100 M_{\odot}$ (Fig. 4). However, we deem a single very massive star progenitor very unlikely for SN 2023fyq for two primary reasons: (1) the estimated ejecta mass is only $0.54 M_{\odot}$ for SN 2023fyq (Dong et al. 2024), significantly lower than expected for a single very massive progenitor; (2) the derived progenitor age from its environment is relatively old and much longer than the typical evolutionary timescale for such very massive stars.

Dong et al. (2024) proposed a binary progenitor system for SN 2023fyq consisting of a low-mass helium star ($\sim 2.5-3 M_{\odot}$) and a compact companion. In their model, mass transfer via Roche-lobe overflow forms an equatorial disk ($\sim 0.6 M_{\odot}$) and an extended envelope ($\sim 0.3 M_{\odot}$). The precursor emission that they have detected is likely to arise from the collision between a disk wind, launched by super-Eddington accretion onto the compact companion, and external material formed from previous mass-transfer outflow. This helium star + compact companion model is also supported by Tsuna et al. (2024) and Baer-Way et al. (2025). In this scenario, the emission of our detected SN progenitor may arise from the same mechanism, i.e. from the collision between a disk wind and external material. Our result also suggests that the precursor emission from the binary interaction has already started as early as ~ 12 yr before the SN explosion, long before the first precursor detection by ground-based telescopes.

SN 2023fyq adds to the diversity of Type Ibn SNe in terms of their progenitor channels and mass-loss mechanisms. For example, the binary companion of the Type Ibn SN 2006jc, discovered by Maund & Ramirez-Ruiz (2016) and Sun et al. (2020), is a non-degenerate supergiant while that of SN 2023fyq is likely a compact object (Dong et al. 2024; Tsuna et al. 2024; Baer-Way et al. 2025). This suggests that their progenitor systems have very different parameters and have undergone very different evolutionary paths. Likewise, the CSM of SN 2006jc was formed via a giant eruption of the progenitor (clearly

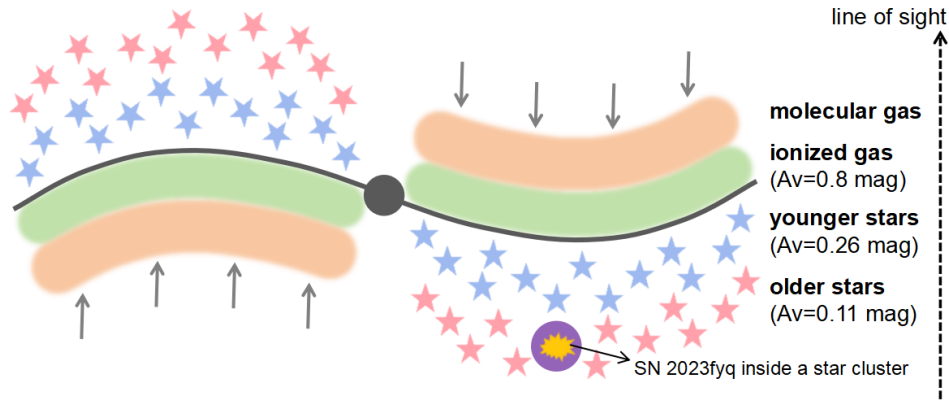


Fig. 8: A schematic diagram illustrating the structure of SN 2023fyq’s host galaxy, NGC 4388, as viewed face-on. The grey arrows show the direction of gas motion.

detected in two years before explosion; Foley et al. 2007; Pastorello et al. 2007) and that of SN 2023fyq was formed via more steady binary mass transfer. These differences indicate that Type Ibn SNe may have remarkable diversities in both progenitor channels and mass-loss mechanisms, the details of which still await further investigations.

Acknowledgements. We are grateful to Dr. César Rojas-Bravo for his helpful comments on this paper. This work is supported by the National Natural Science Foundation of China Grant No.12303051, the Strategic Priority Research Program of the Chinese Academy of Sciences Grant No. XDB0550300, and by the China Manned Space Program Grant No. CMS-CSST-2025-A14. Y.S. acknowledges support from the National Natural Science Foundation of China (NSFC) with grant No. 12303001, and the Fundamental Research Funds for the Central Universities. This work is based on observations made with the NASA/ESA Hubble Space Telescope (Programs 12365, 12185 and 16179) and observations made with the NASA/ESA/CSA James Webb Space Telescope (Programs 2064, 6659 and 5627). The data were obtained from the Space Telescope Science Institute, which is operated by the Association of Universities for Research in Astronomy, Inc., under NASA contract NAS 5–26555 for HST and NASA contract NAS 5-03127 for JWST. This work is also based on observations collected at the European Southern Observatory under ESO programme 108.229J.001 and data obtained from the ESO Science Archive Facility with DOI under <https://doi.org/10.18727/archive/42>. Additionally, this work makes use of the following ALMA data: ADS/JAO.ALMA#2019.1.00763.L, ADS/JAO.ALMA#2023.1.00026.S. ALMA is a partnership of ESO (representing its member states), NSF (USA) and NINS (Japan), together with NRC (Canada), NSTC and ASIAA (Taiwan), and KASI (Republic of Korea), in co-operation with the Republic of Chile. The Joint ALMA Observatory is operated by ESO, AUI/NRAO and NAOJ.

References

- Abdeen, S., Kennefick, D., Kennefick, J., et al. 2020, *MNRAS*, 496, 2, 1610. doi:10.1093/mnras/staa1596
- Asplund, M., Grevesse, N., Sauval, A. J., et al. 2009, *ARA&A*, 47, 1, 481. doi:10.1146/annurev.astro.46.060407.145222
- Baer-Way, R., A. J., N., Jacobson-Galán, W., et al. 2025, *ApJ*, 995, 2, L49. doi:10.3847/2041-8213/ae1cb8
- Baldwin, J. A., Phillips, M. M., & Terlevich, R. 1981, *PASP*, 93, 5. doi:10.1086/130766
- Brennan, S. J., Sollerman, J., Irani, I., et al. 2024, *A&A*, 684, L18. doi:10.1051/0004-6361/202449350
- Bressan, A., Marigo, P., Girardi, L., et al. 2012, *MNRAS*, 427, 1, 127. doi:10.1111/j.1365-2966.2012.21948.x
- Bruzual, G. & Charlot, S. 2003, *MNRAS*, 344, 4, 1000. doi:10.1046/j.1365-8711.2003.06897.x
- Byrne, C. M., Stanway, E. R., Eldridge, J. J., et al. 2022, *MNRAS*, 512, 4, 5329. doi:10.1093/mnras/stac807
- Cai, Y.-Z., Pastorello, A., Maeda, K., et al. 2026, *A&A*, 707, A157. doi:10.1051/0004-6361/202558014
- Cardelli, J. A., Clayton, G. C., & Mathis, J. S. 1989, *ApJ*, 345, 245. doi:10.1086/167900
- Cid Fernandes, R., Mateus, A., Sodré, L., et al. 2005, *MNRAS*, 358, 2, 363. doi:10.1111/j.1365-2966.2005.08752.x
- Crowther, P. A., Schnurr, O., Hirschi, R., et al. 2010, *MNRAS*, 408, 2, 731. doi:10.1111/j.1365-2966.2010.17167.x
- Damas-Segovia, A., Beck, R., Vollmer, B., et al. 2016, *ApJ*, 824, 1, 30. doi:10.3847/0004-637X/824/1/30
- De, K. 2023, *Transient Name Server Discovery Report*, 2023-825, 1.
- Dessart, L., Hillier, D. J., & Kuncarayakti, H. 2022, *A&A*, 658, A130. doi:10.1051/0004-6361/202142436
- Dolphin, A. E. 2000, *PASP*, 112, 776, 1383. doi:10.1086/316630
- Dolphin, A. 2016, *Astrophysics Source Code Library*. ascl:1608.013
- Dong, Y., Tsuna, D., Valenti, S., et al. 2024, *ApJ*, 977, 2, 254. doi:10.3847/1538-4357/ad8de6
- Farias, D., Gall, C., Villar, V. A., et al. 2025, arXiv:2511.12362. doi:10.48550/arXiv.2511.12362
- Fitzpatrick, E. L. 2004, *Astrophysics of Dust*, 309, 33. doi:10.48550/arXiv.astro-ph/0401344
- Foley, R. J., Smith, N., Ganeshalingam, M., et al. 2007, *ApJ*, 657, 2, L105. doi:10.1086/513145
- Font, J., Beckman, J. E., Querejeta, M., et al. 2014, *ApJS*, 210, 1, 2. doi:10.1088/0067-0049/210/1/2
- Fremming, C., Covarrubias, S., Sollerman, J., et al. 2026, arXiv:2603.29043. doi:10.48550/arXiv.2603.29043
- Fujiwara, K., Ueda, Y., Ogawa, S., et al. 2026, arXiv:2604.06719. doi:10.48550/arXiv.2604.06719
- Guérou, A., Krajinović, D., Epinat, B., et al. 2017, *A&A*, 608, A5. doi:10.1051/0004-6361/201730905
- Hong, X., Sun, N.-C., Niu, Z., et al. 2024, *ApJ*, 977, 2, L50. doi:10.3847/2041-8213/ad99da
- Hossein-zadeh, G., Arcavi, I., Valenti, S., et al. 2017, *ApJ*, 836, 2, 158. doi:10.3847/1538-4357/836/2/158
- Hossein-zadeh, G., McCully, C., Zabludoff, A. I., et al. 2019, *ApJ*, 871, 1, L9. doi:10.3847/2041-8213/aafc61
- Hou, L. G. & Han, J. L. 2015, *MNRAS*, 454, 1, 626. doi:10.1093/mnras/stv1904
- Humphreys, R. M. & Davidson, K. 1979, *ApJ*, 232, 409. doi:10.1086/157301
- Karamahmetoglu, E., Taddia, F., Sollerman, J., et al. 2017, *A&A*, 602, A93. doi:10.1051/0004-6361/201629619
- Kewley, L. J., Heisler, C. A., Dopita, M. A., et al. 2001, *ApJS*, 132, 1, 37. doi:10.1086/318944
- Kostiuk, V. S., Marchuk, A. A., & Gusev, A. S. 2024, *Research in Astronomy and Astrophysics*, 24, 7, 075007. doi:10.1088/1674-4527/ad4d3b
- Kostiuk, V., Marchuk, A., Gusev, A., et al. 2025, *Galaxies*, 13, 2, 27. doi:10.3390/galaxies13020027
- Marchuk, A. A. 2024, *A&A*, 686, L14. doi:10.1051/0004-6361/202450602
- Marino, R. A., Rosales-Ortega, F. F., Sánchez, S. F., et al. 2013, *A&A*, 559, A114. doi:10.1051/0004-6361/201321956
- Matheson, T., Filippenko, A. V., Chornock, R., et al. 2000, *AJ*, 119, 5, 2303. doi:10.1086/301352

- Maund, J. R. & Ramirez-Ruiz, E. 2016, *MNRAS*, 456, 3, 3175.
doi:10.1093/mnras/stv2760
- Moriya, T. J., Müller, B., Blinnikov, S. I., et al. 2025, *PASJ*, 77, 6, 1385.
doi:10.1093/pasj/psaf119
- Niu, Z., Sun, N.-C., Maund, J. R., et al. 2023, *ApJ*, 955, 1, L15.
doi:10.3847/2041-8213/acf4e3
- Niu, Z., Sun, N.-C., Zapartas, E., et al. 2026, *ApJ*, 1001, 1, 44. doi:10.3847/1538-4357/ae4bd6
- Osterbrock, D. E. & Ferland, G. J. 2006, .
- Pastorello, A., Smartt, S. J., Mattila, S., et al. 2007, *Nature*, 447, 7146, 829.
doi:10.1038/nature05825
- Pastorello, A., Mattila, S., Zampieri, L., et al. 2008, *MNRAS*, 389, 1, 113.
doi:10.1111/j.1365-2966.2008.13602.x
- Salpeter, E. E. 1955, *ApJ*, 121, 161. doi:10.1086/145971
- Schlafly, E. F. & Finkbeiner, D. P. 2011, *ApJ*, 737, 2, 103. doi:10.1088/0004-637X/737/2/103
- Shivvers, I., Zheng, W., Van Dyk, S. D., et al. 2017, *MNRAS*, 471, 4, 4381.
doi:10.1093/mnras/stx1885
- Smith, N. 2017, *Handbook of Supernovae*, 403. doi:10.1007/978-3-319-21846-5_38
- Sun, N.-C., Maund, J. R., Hirai, R., et al. 2020, *MNRAS*, 491, 4, 6000.
doi:10.1093/mnras/stz3431
- Sun, N.-C., Maund, J. R., Crowther, P. A., et al. 2021, *MNRAS*, 504, 2, 2253.
doi:10.1093/mnras/stab994
- Sun, N.-C., Maund, J. R., Crowther, P. A., et al. 2022, *MNRAS*, 510, 3, 3701.
doi:10.1093/mnras/stab3768
- Sun, N.-C., Maund, J. R., Shao, Y., et al. 2023, *MNRAS*, 519, 3, 3785.
doi:10.1093/mnras/stac3773
- Sun, N.-C., Maund, J. R., & Crowther, P. A. 2023, *MNRAS*, 521, 2, 2860.
doi:10.1093/mnras/stad690
- Tsuna, D., Wu, S. C., Fuller, J., et al. 2024, *The Open Journal of Astrophysics*, 7, 82. doi:10.33232/001c.123897
- Tully, R. B., Courtois, H. M., & Sorce, J. G. 2016, *AJ*, 152, 2, 50.
doi:10.3847/0004-6256/152/2/50
- Valerin, G., Benetti, S., Elias-Rosa, N., et al. 2023, *Transient Name Server Classification Report*, 2023-1777, 1.
- Veilleux, S., Bland-Hawthorn, J., Cecil, G., et al. 1999, *ApJ*, 520, 1, 111.
doi:10.1086/307453
- Walmswell, J. J., Eldridge, J. J., Brewer, B. J., et al. 2013, *MNRAS*, 435, 3, 2171.
doi:10.1093/mnras/stt1444
- Wang, Z.-Y., Pastorello, A., Maeda, K., et al. 2024, *A&A*, 691, A156.
doi:10.1051/0004-6361/202451131
- Wang, Z.-Y., Pastorello, A., Cai, Y.-Z., et al. 2025, *A&A*, 700, A156.
doi:10.1051/0004-6361/202554768
- Xi, Q., Sun, N.-C., Zhao, Y.-H., et al. 2025, *MNRAS*, 542, 3, 1852.
doi:10.1093/mnras/staf1275
- Xi, Q., Sun, N.-C., Zhao, Y., et al. 2026, *arXiv:2604.03032*.
doi:10.48550/arXiv.2604.03032

Appendix A: Decontamination of neighboring sources

Since the HST/WFC3/IR images have a relatively lower spatial resolution, the SN progenitor may be blended with close neighboring stars and its photometry could be contaminated. As shown in Fig. A.1, the pixel size of HST/WFC3/IR (0.12") is much larger than those of HST/WFC3/UVIS and JWST/NIRCam (0.04" and 0.031", respectively). On the higher-resolution HST/WFC3/UVIS and JWST/NIRCam images, four distinct sources can be detected at or near the SN position (*Sources A, B, C and D*). Using coordinate transformation matrices, we register the positions of these sources on all observations. We find that on the lower-resolution HST/WFC3/IR images, while *Source C* and *Source D* can still be marginally resolved, *Source A* and *Source B* are completely blended and the photocenter of the blended source lies between the two sources. Therefore, photometry of the SN progenitor is mainly affected by the contamination of *Source B*. Accordingly, we perform a linear interpolation of the flux of *Source B* across the F814W and F182M bands to estimate its brightness in the F110W and F160W bands and we consider two extremes, in which *Source B* contributes no or all of its brightness to the total photometry of the SN progenitor. In this way, we can estimate and remove the contamination in the photometry and the range spanned by the two extremes is taken as the error bar associated with the data points in Fig. 2).

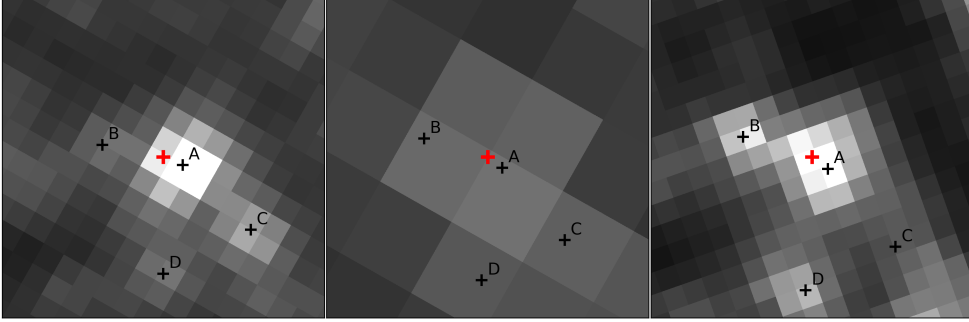


Fig. A.1: Images observed by HST/WFC3/UVIS/F814W (left), HST/WFC3/IR/F110W (middle) and JWST/NIRCam/F182M (right) near the SN site. The red "+" symbols are the photo-center of the SN progenitor detected on HST/WFC3/IR/F110W image. The black "+" symbols are the centers of the *Sources A, B, C and D* detected on the other two higher-resolution panels. We used common stars to compute the coordinate transformation matrices and mark the above source positions on all panels.

Appendix B: VLT/MUSE spectral line fitting

Since NGC 4388 is an edge-on galaxy, the substantial line-of-sight superposition of distinct gaseous components across the galaxy gives rise to complex emission-line profiles in our measurements. Emission lines along the spiral arms typically display a single kinematic component, while those in the nuclear region exhibit 2–4 distinct components. We present four example regions with different numbers of spectral line components; their positions within the host galaxy and the corresponding Gaussian fitting results for the emission lines are shown in Fig. B.1.

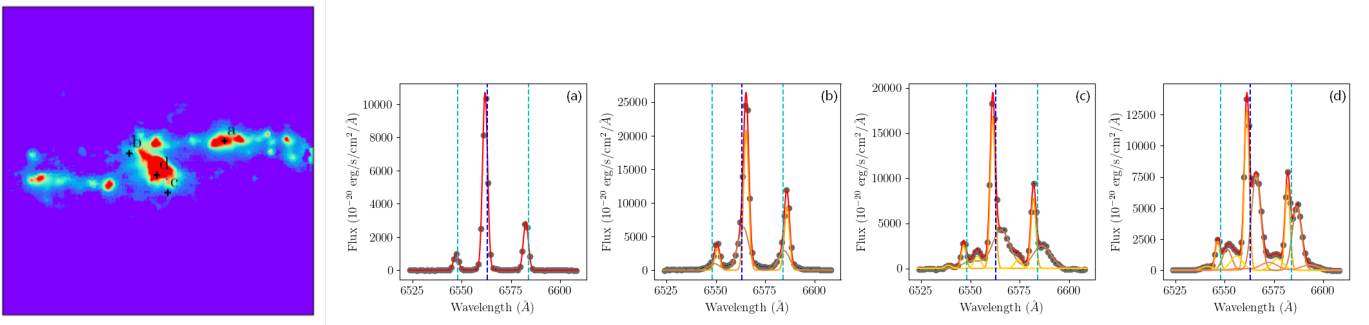


Fig. B.1: The wavelength-integrated flux map of the H α line total emission observed by VLT/MUSE and spectral line fitting results with 1, 2, 3, 4 components corresponding to the four positions marked by the "+" symbols (i.e. a, b, c and d, respectively).

Appendix C: BPT diagram

Fig. C.1 shows the BPT diagram (Baldwin et al. 1981) with the maximum starburst line defined by Kewley et al. (2001). The BPT diagram is a powerful optical diagnostic tool to distinguish the dominant ionization mechanism of ionized gas. With this diagram, we found that the spiral arms are ionized by star formation while the nuclear region is ionized by AGN.

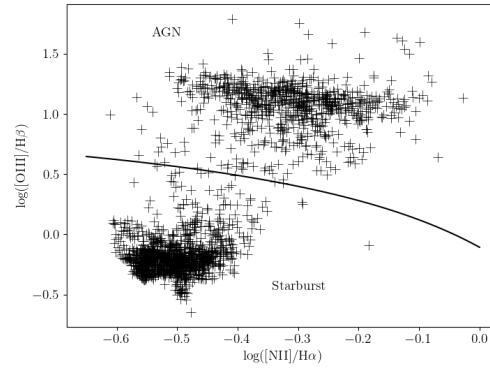


Fig. C.1: BPT diagram of NGC 4388. The black line is the maximum starburst line defined by Kewley et al. (2001).